J Electroceram (2012) 29:106–116
DOI 10.1007/s10832-012-9755-y

Exhaled VOCs sensing properties of WO_3 nanofibers functionalized by Pt and IrO_2 nanoparticles for diagnosis of diabetes and halitosis

Jungwoo Shin · Seon-Jin Choi · Doo-Young Youn · Il-Doo Kim

Received: 20 July 2012 / Accepted: 31 July 2012 / Published online: 16 August 2012

Abstract This work presents a simple synthetic route to produce WO_3 nanofibers functionalized by catalytic Pt and IrO_2 nanoparticles and their superior acetone and H_2S sensing characteristics, demonstrating the potential use of Pt and IrO_2 nanoparticles in applications as sensors of biomarkers of diabetes and halitosis, respectively, in exhaled breath. The individual WO_3 fiber, calcined at 500 °C, was composed of small nanoparticles with a size distribution in the range of 30–100 nm. Networks of WO_3 fibers exhibited a high surface-to-volume ratio and unique morphologies, thus facilitating efficient gas transport into the entire fiber layers. Pt (4–7 nm) and Ir (4–8 nm) nanoparticles were synthesized by polyol methods and were used as additives to decorate the surface of the WO_3 fibers. After a heat treatment, those catalyst particles were partially or fully oxidized to Pt/PtO_x and IrO_2, respectively. To investigate the advantages of Pt-decorated WO_3 fibers (Pt-WO_3) and IrO_2-decorated WO_3 (IrO_2-WO_3) fibers as acetone (CH_3COCH_3) and H_2S sensing materials, respectively, we carried out gas-sensing measurements in a highly humid atmosphere (RH 75 %) similar to that of an oral cavity. The Pt-WO_3 fibers showed a high acetone response (R_{air}/R_{gas}=8.7 at 5 ppm) at 350 °C and a superior H_2S response (R_{air}/R_{gas}=166.8 at 5 ppm) at 350 °C. Interestingly, IrO_2-WO_3 fibers showed no response to acetone, while the gas response to H_2S exhibited temperature-insensitivity, which has never been reported in any other work. Thus, the highly selective cross-response between H_2S and acetone was successfully achieved via the combination of IrO_2 particles on WO_3 fibers. This work demonstrates that accurate diagnosis of diabetes and halitosis by sensing exhaled breath can be realized through the use of electrospun WO_3 fibers decorated with Pt and IrO_2 catalysts.

J. Shin · S.-J. Choi · D.-Y. Youn · I.-D. Kim (✉)
Department of Materials Science and Engineering,
Korea Advanced Institute of Science and Technology,
Daejeon 305-701, Republic of Korea
e-mail: idkim@kaist.ac.kr

Keywords Electrospinning · Nanofibers · Exhaled breath sensors · WO_3 · Pt · IrO_2 · Diabetes · Halitosis

1 Introduction

Recently, exhaled breath sensors have been attracted much attention due to their ability to provide facile diagnosis of diabetes [1, 2], halitosis [3–5], and certain diseases through the simple detection of exhaled volatile organic compounds (VOCs), typically acetone and H_2S. For instance, the acetone level in breath is closely related to diabetes, because incomplete management of glucose in the blood of diabetes patients can result in the production of higher levels of acetone (>1.8 ppm) in exhaled breath compared to that of healthy people (<0.9 ppm) [6]. In addition, H_2S can be produced by the micro-bacterial metabolism of amino acids and proteins in the digestive tract [7, 8] and can be used as a target gas for diagnosis of halitosis, or oral malodor. The main advantages of exhaled breath sensors are simplicity of operation, non-invasiveness, a low cost, and rapid detection. While many diabetes patients must undergo periodic blood sugar testing, the use of real-time exhaled breath sensors for monitoring acetone levels can significantly reduce both the pain felt during these tests and the time required to conduct them. In addition, quantitative measurements of H_2S in exhaled breath for malodor intensity monitoring purposes would be beneficial for preventing the relapse of this and other diseases and would allow the formulation of proper drug therapies. In this sense, the most challenging issues related to the development of exhaled breath sensors include optimizing the designs of materials and structures with high gas sensitivity and the selection of specific target gases.

To obtain outstanding gas-sensing performance, numerous studies have been conducted in an effort to develop highly sensitive metal oxide chemiresistive sensors using one-

dimensional (1-D) nanostructures such as nanowires [9], nanotubes [10], nanorods [11], or nanowhiskers [12]. Among the different strategies for producing 1-D sensing materials, electrospinning offers several unique advantages, including a simple fabrication process and reproducible device performance due to the characteristics of the fiber network [13]. In particular, nanofibrous metal oxide layers display unique polycrystalline morphologies; i.e., the nanofibers are composed of tiny nanoparticles that give rise to a large surface-to-volume ratio, leading to the effective gas modulation of the fiber-based sensing layers [14]. Specifically, the bimodal architecture, which includes large pores separating the nanoscale fibers and small pores that form among densely packed nanoparticles, is one of the unique morphological advantages of electrospun metal-oxide fibers.

Thus far, a number of electrospun metal-oxide nanofibers have been synthesized and studied. These metal-oxide nanofibers include SnO_2 [15], TiO_2 [16], ZnO [17], MoO_3 [18], In_2O_3 [19], Zn_2SnO_4 [20] and WO_3 [21]. Among the various types of metal oxides, n-type WO_3, with a wide band gap of 2.6 eV, is considered as a prospective candidate material for sensing VOCs due to its good electrical properties, excellent gas-sensing characteristics and its nontoxicity [22, 23]. Compared to other oxides, the interesting features of WO_3 are closely related to its stoichiometric phase transition and specific affinity toward certain gases, as changes in its phase lead to distinguishable variations in its electrical and optical properties [24–26]. Thus far, several gas sensor works using electrospun WO_3 fibers have been reported. Examples include those by Wang et al. [27], Santucci et al. [28], Gouma et al. [29], Zhang et al. [30], and Kim et al. [31]. All measurements in this studies were conducted in a dry air condition for the detection of environmental gases such as NO_x, $CO_{x\ (x=1,2)}$, C_2H_4 and NH_3. Although some articles related to exhaled breath sensors using WO_3 nanoparticles [32–34], thin film [35] and nano-rods [36] have been published, to the best of our knowledge, there are no reports about the potential use of electrospun WO_3 fibers, particularly those decorated with catalytic additives, as an exhaled breath sensor for the diagnosis of diabetes and halitosis.

Thus, for the first time, we report here the facile synthesis and superior acetone and H_2S sensing properties of WO_3 fibers functionalized by Pt and IrO_2 particles. The unique sensitization effects of Pt and IrO_2 catalysts anchored onto the surface of WO_3 fibers are clearly discussed in terms of their superior response and cross-sensing properties against acetone and H_2S. The temperature-independent gas response characteristics of IrO_2-WO_3 against H_2S gas in the range of 350–500 °C are highlighted. Based on these results, we expect that the process of the facile pattern recognition of acetone and H_2S in exhaled breath can be simplified through the use of metal-oxide fibers functionalized by specific catalysts, thus real-time diagnosis of diabetes and halitosis can be facilitated.

2 Experimental

2.1 Synthesis of WO_3 fibers

All chemicals were used as received without any purification. Polycrystalline WO_3 fibers were prepared by the electrospinning of WCl_6 precursors dissolved in a polyvinylpyrrolidone (PVP) solution and a subsequent calcination step in an air atmosphere. In a typical procedure, 1.5 g of WCl_6 and 1.25 g of PVP (Mw=1,300,000 g mol^{-1}) were dissolved in 10 g of dimethyl formamide (DMF) and 0.2 g of acetic acid. After vigorous stirring at 500 rpm for 10 h at room temperature, the WCl_6/PVP solution was loaded into a plastic syringe connected to a 21-gauge needle at a constant flow rate (5 μl min^{-1}). High voltage (11.5 kV) and a constant distance (15 cm) were maintained between the syringe tip and the collecting stainless steel foil, which was wrapped around a grounded rotating cylinder (100 rpm). The collected WCl_3/PVP composite fibers were heat-treated at 500 °C for 3 h in an electric furnace (Vulcan 3-550, Ney) to ensure the complete burning out of polymers and to induce crystallization of the WO_3 fibers. The heating rate was fixed at 4 °C min^{-1} and the cooling rate was maintained at 20 °C min^{-1}.

2.2 Synthesis of Pt nanoparticles

Pt catalytic nanoparticles were synthesized by a polyol method [37]. 0.5 g of H_2PtCl_6 was dissolved in 5 ml ethylene glycol (EG) solution. Then, the H_2PtCl_6/EG solution was slowly injected into a three-neck round flask filled with 45 ml of EG in a heated oil bath (150 °C). Subsequently, 20 ml of PVP (0.5 g, 10,000 g mol^{-1}) dissolved in an EG solution was added to the flask at a rate of 2 ml min^{-1}. The color of the solution turned suddenly from yellow to black. After 1 h, acetone was added to the solution at a 5:1 volume ratio of acetone to the Pt solution. To isolate the Pt particles from the solvent, the mixed solution was centrifuged at 3000 rpm for 5 min and washed with deionized (DI) water multiple times. The obtained black powders were dispersed in ethanol, resulting in the formation of a Pt colloidal solution, which was directly used as the Pt additive source.

2.3 Synthesis of Ir nanoparticles

To decorate the surface of the WO_3 fibers with the IrO_2 catalyst, Ir catalytic nanoparticles were synthesized by the polyol method described above. 0.5 g of H_2IrCl_6 was dissolved in 75 mL EG under magnetic stirring at room temperature. The H_2IrCl_6 solution was then heated to 100 °C at a rate of 1 °C min^{-1} for 1 h. The color of the solution changed gradually from dark to light brown. To obtain colloidal Ir particles, the synthesized solution was centrifuged at 3000 rpm for 10 min and was then washed with DI water multiple times. Ir nanoparticles were

dispersed in ethanol, and these were directly used as the Ir additive source. Finally, IrO_2 catalysts were formed after high-temperature calcination of the Ir-decorated WO_3 fibers.

2.4 Microstructural characterizations

The microstructural characteristics of the as-spun WCl_6/PVP fibers and calcined WO_3 fibers were investigated using a scanning electron microscope (Field Emission SEM, Magellan400, FEI) and a transmission electron microscope (FE-TEM 200KV, Tecnai). The characterization of the crystal structures of the calcined WO_3 fibers was carried out by X-ray diffractometry (XRD, D/MAX-2500 series, RIGAKU; with CuKα radiation (λ=1.54 Å)). The morphological distribution of the Pt and IrO_2 particles on the WO_3 fibers and the oxidation states were identified by high-resolution transmission electron microscopy (HRTEM) and X-ray photoelectron spectroscopy (XPS, Sigma Probe, Thermo VG Scientific), respectively.

2.5 Fabrication of sensors

To investigate the acetone and H_2S gas-sensing properties of pristine WO_3, Pt-WO_3 fibers, and IrO_2-WO_3 fibers, three different fibers, which were mixed with a polymeric binder (PVAc), were coated onto Al_2O_3 substrates patterned with two Au electrodes accompanied with an electric heater on the back side. In this study, colloidal Pt and Ir nanoparticles dispersed in ethanol were mixed with WO_3 fibers using a pestle and a mortar and were dropped onto the sensing substrate, compressed on a pre-heated hot plate (80 °C) for 30 min. Next, the WO_3, Pt-WO_3 and IrO_2-WO_3 fibers on each sensor substrate were heat-treated at 500 °C for 2 h to eliminate the PVAc and thus provide good electrical contact between the network of the WO_3 fibers and the Au electrodes. During this process, Ir nanoparticles were oxidized to IrO_2 as well.

2.6 Gas-sensing test

Exhaled breath sensing tests against the two target gases (acetone and H_2S) at various concentrations (5–1 ppm) were performed to evaluate the acetone and H_2S sensing performance of the WO_3, Pt-WO_3, and IrO_2-WO_3 fibers in an operating temperature range of 300–500 °C. To identify the gas response characteristics of our sensors in a highly humid atmosphere, humid air was injected to the testing chamber, and a relative humidity of 75 % was maintained (RH 75 %). Prior to the sensor test, networks of WO_3, Pt-WO_3, and IrO_2-WO_3 fibers were stabilized for 48 h until a constant resistivity level was obtained. The target gases were then introduced into the testing chamber for 10 min. This was followed by purging with air for 10 min to clear the target gas.

The responses of the sensors were evaluated by measuring the resistivity changes using a 16-channel multiplexer (34902A, Agilent) combined with a data acquisition system (34972A, Agilent). The temperature of the sensors was controlled by a DC power supply (E3647A, Agilent) with applied bias through a heater.

3 Results and discussion

Figure 1(a) shows a scanning electron microscope (SEM) image of the as-spun WCl_6 precursors/PVP composite fibers, showing their average diameter of 370 nm (standard deviation (STDEV): 1.28). Some portions of the composite fibers have thin, ribbon-like morphology of the type often observed in electrospun fibers, presumably originating from the skin collapse mechanism driven by either uneven evaporation of the solvent or coulombic repulsion between the jets and the surface [38]. To be specific, the ribbon was created by the condensation and gelation of the polymers and precursors at the outermost parts of the fibers, which were exposed to air after the evaporation of the solvent inside the fiber [39]. After the calcination process, the average diameter (285 nm, STDEV: 2.00) of the WO_3 fibers was slightly reduced due to the densification of WO_3 crystallites and the burning out of the polymers (Fig. 1(b)). The magnified SEM image in Fig. 1(c) reveals that the calcined WO_3 fibers are composed of nanoparticles (30–100 nm). A number of small pores, which existed among packed particles, arose due to the growth of the relatively large WO_3 particles. These small pores as well as large voids made by the fiber networks can provide fast gas diffusion pathways for gas molecules into the inside surface of the fibers, thereby enhancing the gas responses. Figure 1(d) exhibits a transmission electron microscope (TEM) image of a calcined WO_3 fiber. Small pores are clearly observable among the loosely packed WO_3.

To investigate the crystal structure of the WO_3 fibers, we carried out an XRD analysis. Distinct characteristic peaks ((002), (020) and (200)) were clearly observed; these correspond to the monoclinic WO_3 lattices with a space group of $P2_1/n$ according to JCPDS (PDF #43-1035) (Fig. 2).

We synthesized Pt and Ir nanoparticles via a polyol method to investigate the effect of an addition of catalytic Pt and IrO_2 nanoparticles onto WO_3 fibers for sensing acetone and H_2S. Figure 3(a) shows a TEM image of the as-prepared Pt nanoparticles, which have diameters of 4–7 nm. Figure 3(b) is a TEM image of the as-prepared Ir nanoparticles (4–8 nm). These nanoparticles were mixed with calcined WO_3 fibers using PVAc as a binder and were then drop-coated onto sensor substrates. After a heat treatment at 500 °C, partial oxidation of Pt and the complete oxidation of the Ir particles were observed, resulting in the formation of PtO and IrO_2 species, respectively (Figs. 3(c) and (d)). The yellow circles in Fig. 3(c) indicate that the Pt nanoparticles are well dispersed on the surface of the WO_3 fibers without severe aggregation.

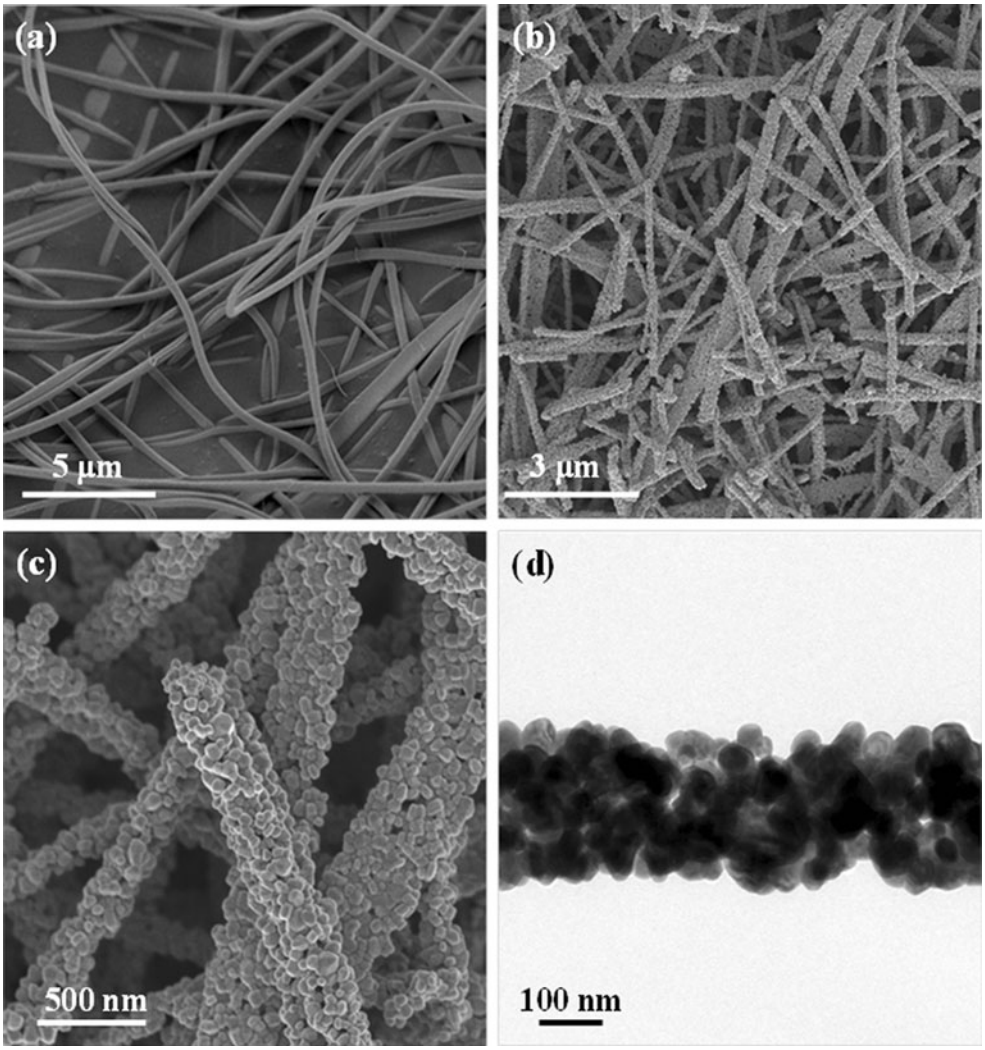

Fig. 1 (**a**) A SEM image of the as-spun WCl_6 precursor/PVP composite fibers; (**b**) a SEM image of calcined WO_3 fibers; (**c**) a magnified SEM image of calcined WO_3 fibers; and (**d**) a TEM image of single WO_3 fiber

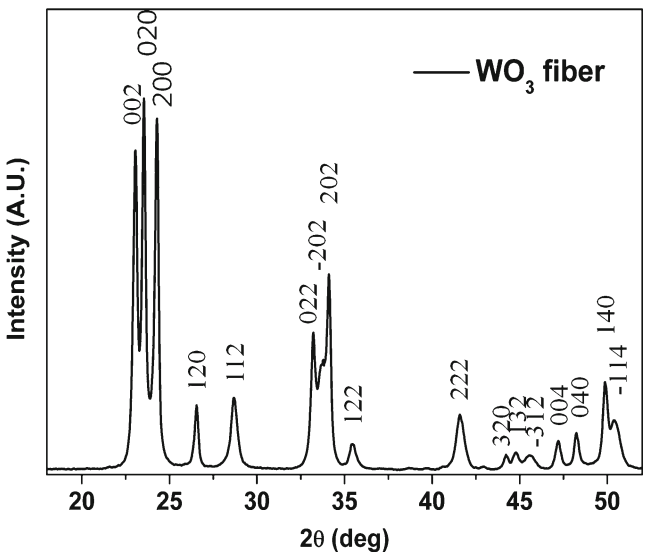

Fig. 2 X-ray diffraction pattern of calcined WO_3 fibers

Meanwhile, the IrO_2 particles, shown in the green circles in Fig. 3(d), indicate that the IrO_2 particles (10–40 nm) aggregated slightly on the WO_3 fibers, not overly uncommon considering the sizes of the as-prepared Ir particles (4–8 nm). The green circles in the inset of Fig. 3(d) indicate that the IrO_2 particles grew in the form of small sprouts on the WO_3 crystals. It is presumed that the oxidation of Ir nanoparticles during the heat treatment had the effect of elongating the growth of IrO_2 particles in the vertical direction of the WO_3 surface with a preferential direction of (001) [40]. Figure 3(e) and (f) reveal the surface of a WO_3 crystal decorated with Pt and IrO_2 particles, respectively. The HRTEM image in Fig. 3(e) shows a lattice distance of 0.383 nm for the WO_3 crystal, which corresponds to monoclinic WO_3. The inset is a Fast Fourier Transform (FFT) image of the WO_3 crystal. The calculated pattern clearly displays the (002) and (200) planes of the WO_3 crystals. The lattice distance of the (111) plane of Pt (0.226 nm) is also shown in the figure [27]. Figure 3(f) shows the (110) and (001) lattices of IrO_2, showing its rutile crystal structure [40].

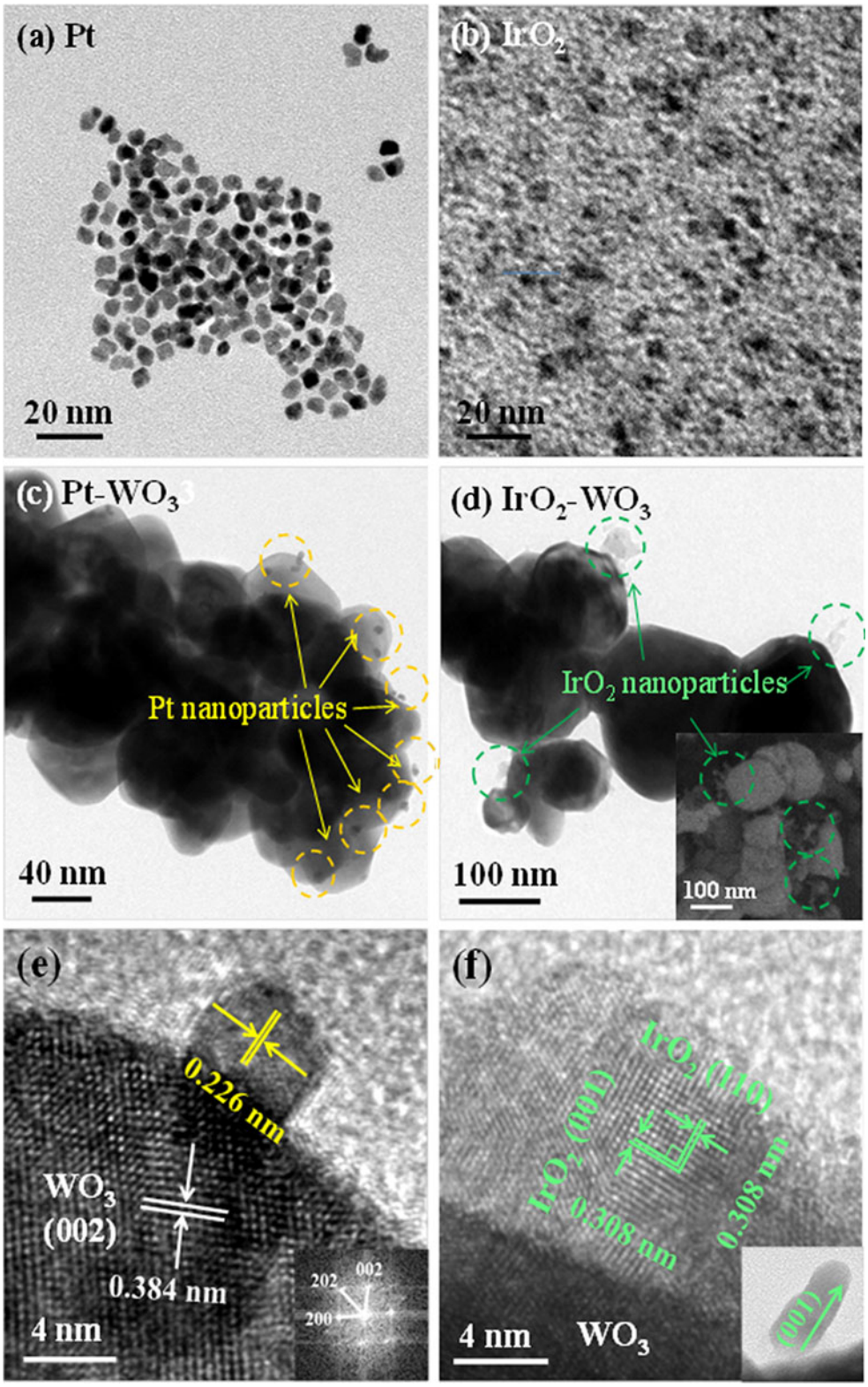

Fig. 3 TEM images of polyol synthesized (**a**) Pt nanoparticles and (**b**) Ir nanoparticles, (**c**) Pt-WO_3 and (**d**) IrO_2-WO_3 nanofibers. Yellow and green circles in (c) and (d) denote the existence of Pt and IrO_2 particles on WO_3 fibers. Inset of Fig. 3d indicates that the shape of IrO_2 is similar to the elongated rods. (**e**) HRTEM image of Pt-WO_3 fiber. The inset shows Fast Fourier Transform (FFT) pattern of a WO_3 crystal. (**f**) HRTEM image of IrO_2-WO_3 fiber. The inset shows IrO_2 particles attached on WO_3 fibers grown on (001) direction

To investigate the oxidation states of the elements comprising the Pt-WO_3 and IrO_2-WO_3 fibers, an XPS analysis was carried out. The characteristic peaks of the Pt-WO_3 fibers, ranging from 0 eV to 650 eV, are displayed in Fig. 4(a). Three main compounds, W, O, and Pt, were clearly identified from the XPS spectra. The peaks corresponding to the energy levels of Pt $4f_{5/2}$ and Pt $4f_{7/2}$ are shown in Fig. 4(b). The wide spectra of the oxidized Pt state assigned to 72.2 and 75.5 eV along with

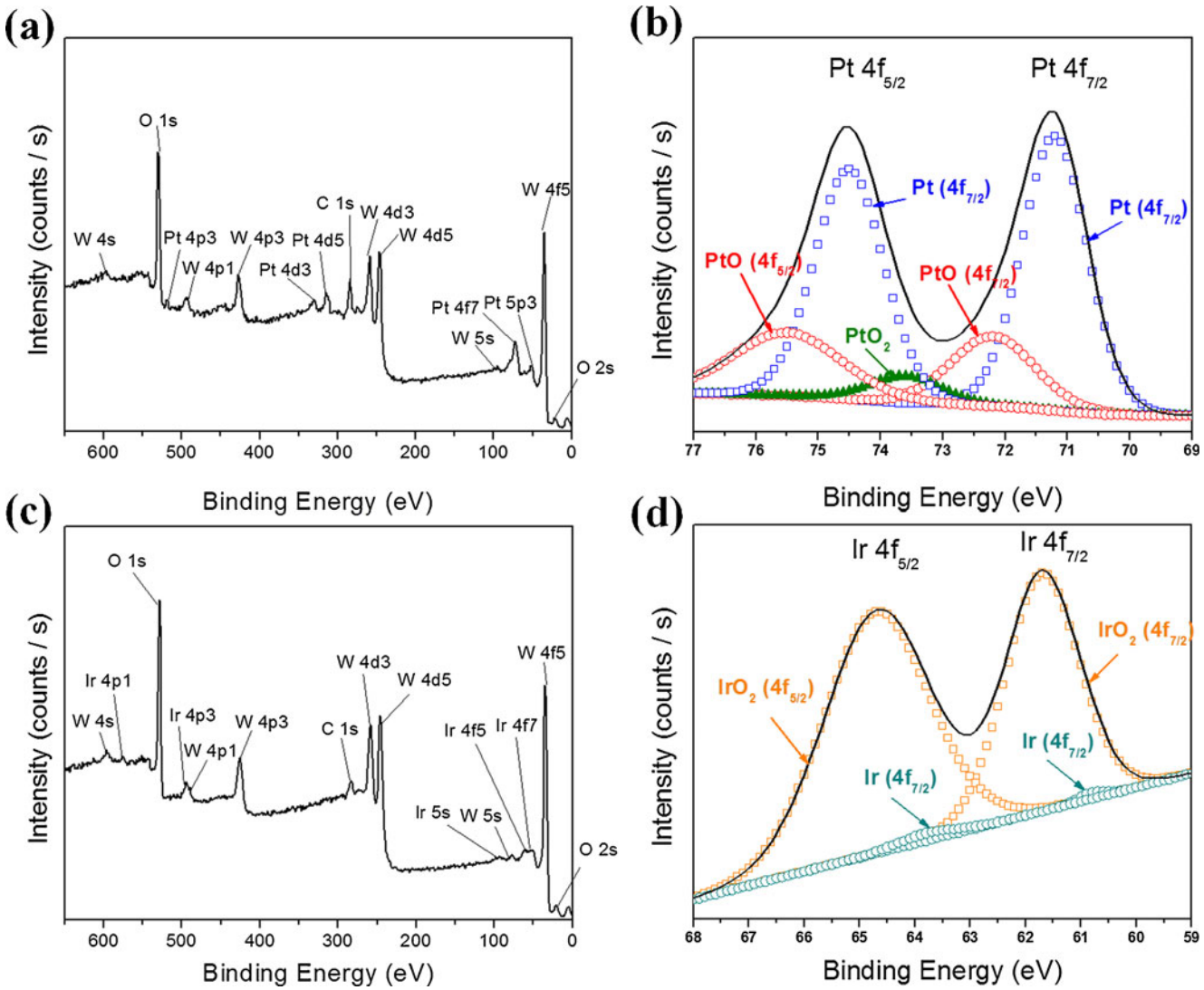

Fig. 4 X-ray photoelectron spectroscopy spectra of (**a**) Pt-WO_3 fibers and (**b**) analysis of Pt $4f_{5/2}$ and $45f_{7/2}$ energies that are related to the oxidation state of Pt and PtO; and XPS spectra of (**c**) IrO_2-WO_3 fibers and (**b**) analysis of Ir $4f_{5/2}$ and $45f_{7/2}$ energies that are related to the oxidation state of Ir and IrO_2

sharp peaks of metallic Pt at 71.2 and 74.5 eV indicate that Pt was partially oxidized by the thermal treatment at 500 °C. While WO_3 has a band-energy gap of 2.585 eV due to O_{2p}-W_{5d} transitions, the oxidized Pt, i.e., the PtO phase, has a p-type semiconductor property (bandgap=0.86 eV) [41], which can give rise to the formation of p-n junctions. The entire range of the XPS spectra of the IrO_2-WO_3 fibers is shown in Fig. 4(c). The strong peaks at 61.7 and 64.7 eV correspond to the oxidized state of Ir, or Ir^{4+}, which is in good agreement with the results for IrO_2, while the metallic peaks of Ir, at 60.8 and 63.8 eV, remain negligible. IrO_2 exhibits n-type semiconductor properties with a band gap of 2.34 eV [42].

Prior to the evaluation of the gas-sensing performances, the initial resistivity values of the WO_3, Pt-WO_3, and IrO_2-WO_3 fibers were measured as a function of the temperature (Table. 1). Generally, the initial resistivity decreases as the temperature increases. One interesting characteristic related to the resistivity

Table. 1 A list of initial resistivities (R_{air}) under humid air atmosphere of pristine WO_3, Pt-WO_3, and IrO_2-WO_3 fibers as a function of operating temperatures

Temperature	Resistivity (MΩ)		
(°C)	WO_3 fibers	Pt-WO_3 fibers	IrO_2-WO_3 fibers
300	1.599	73.053	1.950
350	1.560	70.047	2.018
400	1.3135	32.164	2.280
450	0.894	8.058	2.172
500	0.485	2.812	1.944

change was observed in the catalyst-decorated WO_3 fibers. The Pt-WO_3 fibers showed a dramatic increase in their initial resistivity when compared to pristine WO_3 fibers. Whereas pristine WO_3 and IrO_2-WO_3 fibers showed corresponding initial resistivity values of 1.599 MΩ and 1.950 MΩ, the Pt-WO_3 fibers had high resistivity of 73.053 MΩ at 300 °C. This result can be attributed to the formation of depletion layers from the p-n junction between p-type PtO (0.86 eV) and n-type WO_3 (2.6 eV) [43]. More importantly, Pt nanoparticles coated onto WO_3 fibers can facilitate oxygen adsorption by means of chemical sensitization, which takes electrons from the conduction band of the WO_3 fibers, thereby dramatically increasing the resistivity. IrO_2-WO_3 fibers represent a much lower initial resistivity than Pt-WO_3 fibers, mainly due to the high conductivity of the n-type semiconductor IrO_2 [42], despite the fact that a slight increase in the resistivity compared to pristine WO_3 was observed as a result of the sensitization process. As the temperature increased, the resistivity of the WO_3 and Pt-WO_3 fibers decreased due to the increase in the thermally excited electrons in the materials. Pt-WO_3 in particular showed a dramatic decrease in its resistivity above 350 °C. The rapid decrease in the resistivity of the Pt-WO_3 fibers can be attributed to oxygen desorption on the WO_3 fibers at a high temperature, which releases electrons into the conduction band of the WO_3. On the other hand, the initial resistivity levels of IrO_2-WO_3 remained constant independent of the temperatures through the entire range.

For an accurate diagnosis of diabetes and halitosis in clinical applications, gas sensors using WO_3, Pt-WO_3, and IrO_2-WO_3 fibers were tested and analyzed under fluid changes at concentrations of 5, 4, 3, 2, and 1 ppm of acetone and H_2S in a humid atmosphere (Fig. 5). As shown in Fig. 5 (a), Pt-WO_3 fibers measured at 350 °C showed a slightly higher acetone response (R_{air}/R_{gas}=8.2 at 5 ppm) compared to that (R_{air}/R_{gas}=5.2 at 5 ppm) of pristine WO_3 fibers. At a low concentration, the acetone response of Pt-WO_3 fibers decreased to a response level similar to that of pristine WO_3 fibers (R_{air}/R_{gas}=3.65) at 1 ppm, which means that Pt decoration has an influence exclusively on the high concentration of acetone. To address this phenomenon, the role of Pt catalyst on the metal oxide surface should initially be identified. For Pt catalyst as an additive, the chemical sensitization mechanism is dominant over electrical sensitization and hence strongly affects the resistivity of Pt-WO_3 fibers by the adsorption-diffusion reaction [44]. The Pt catalyst can dissociate the adsorbed oxygen and lead to diffusion toward the metal-oxide surface via a spillover process [45], thereby inducing a large amount of oxidized-state oxygen (O^-, O^{2-}) on the surface. When exposed to reducing gases such as acetone and H_2S, surface-adsorbed oxygen on Pt-WO_3 fibers can be released in the form of CO_2 or H_2O [23, 46], leaving electrons behind in the WO_3 fibers. Thus, the remarkable resistivity changes caused by the released electrons can lead to a higher response in Pt-WO_3 fibers as compared to pristine WO_3 fibers because the dissociating and capturing of oxygen on the surface cannot be assisted by catalysts. The plausible reason for the smaller response of Pt-WO_3 below 2 ppm is related to the contribution of excessively adsorbed oxygen. By means of chemical sensitization, Pt can introduce a great amount of adsorbed oxygen. Acetone molecules at a high concentration can react with Pt-introduced adsorbed oxygen. At a low concentration of acetone, however, a certain amount of adsorbed oxygen remained uninfluenced; thus, relatively few electrons can be released into the conduction band of WO_3. At an elevated temperature of 400 °C, the responses of the pristine WO_3 and Pt-WO_3 fibers were reversed. The responses of pristine WO_3 fibers showed an enhanced response to acetone (R_{air}/R_{gas}=3.12), even at 1 ppm (Fig. 5(b)), while the response of Pt-WO_3 became much lower. On the other hand, the acetone response of the IrO_2 - WO_3 fibers was scarcely detected, as shown in Figs. 5(a) and (b).

The acetone responses of pristine WO_3 fibers and Pt-WO_3 fibers at various temperatures in the range of 300–500 °C are summarized in Fig. 5(c). Pt-WO_3 fibers demonstrate declining response behaviors after an increase in the operating temperature, while pristine WO_3 fibers exhibit increasing response behaviors after an increase in the operating temperature. It was determined that the responses of pure WO_3 fibers gradually increase from 300 °C and reach a maximum at an operating temperature in the range of 400–450 °C. In contrast, Pt-WO_3 fibers exhibit their maximum responses at 350 °C, and showing dramatic decreases in these levels as the temperatures increase beyond this point. The reason behind the different optimum operating temperatures is the Pt catalyst effect, which modifies the operating temperature, or generally lowers the optimum temperature and enhances the sensor sensitivity [47, 48]; at elevated temperatures, the chemisorbed oxygen, which is driven by the chemical sensitization of Pt, can easily be vaporized and dissociated, thereby lowering the resistivity and resulting in decreased responses of Pt-WO_3 fibers.

On the other hand, the increased response of pure WO_3 fibers with an increase in the temperature can be explained by the thermally excited electrons which jump from the valence band to the conduction band. This promotes enhanced resistivity changes in presence of reducing gases, i.e., acetone and H_2S. It was also revealed that the IrO_2-WO_3 fibers do not react with acetone at appreciable levels. In other words, at high-temperature oxygen desorption reaction is predominant, especially for Pt-WO_3 fibers with excessive amounts of adsorbed oxygen. Thus, the oxygen desorption process is hence the more thermodynamically favorable process, causing the gas responses at high temperatures for Pt-WO_3 fibers to be greatly reduced.

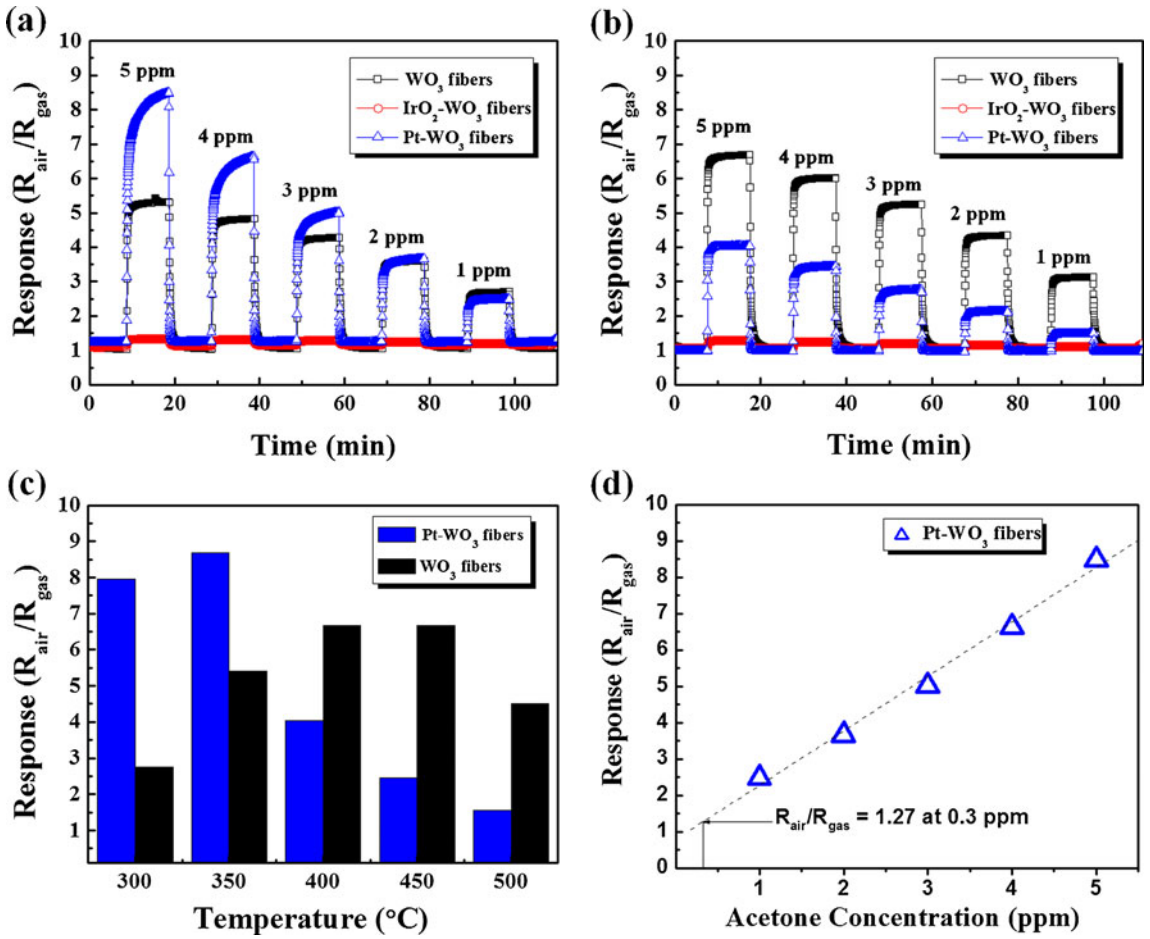

Fig. 5 The cyclic acetone response (R_{air}/R_{gas}) of WO_3, Pt-WO_3, and IrO_2-WO_3 fibers at (**a**) 350 °C and (**b**) 400 °C under acetone concentrations (5, 4, 3, 2 and 1 ppm). (**c**) Acetone responses of WO3 and Pt-WO_3 fibers as various temperatures (300–500 °C) at 5 ppm, (**d**) The linear extended acetone response of Pt-WO_3 fibers at 350 °C

Figure 5(d) shows the linear extended acetone response of Pt-WO_3 fibers at 350 °C. The calculated acetone response (R_{air}/R_{gas}) of the Pt-WO_3 fibers was 1.27 at 0.3 ppm, which can distinguish diabetes patients whose acetone concentrations exceed 1.8 ppm as compared to healthy people (<0.9 ppm).

The responses of the fabricated sensors to H_2S gas were also assessed, as presented in Fig. 6. The gas-sensing result showed that Pt-WO_3 fibers exhibited the highest response to H_2S at 350 °C (R_{air}/R_{gas}=166.8 at 5 ppm) (Fig. 6(a)). It also revealed that the gas response of Pt-WO_3 fibers to H_2S was 19 times higher than that of acetone (166.8 versus 8.7). The cause of the superior gas responses of the Pt-WO_3 fibers in H_2S over acetone is the complexity of the reaction and reaction speed difference between the acetone molecule and the H_2S. Because acetone molecules require more complex reactions composed of multiple steps of dissociating reducing species and producing intermediate compounds with respect to different speeds, chemisorbed oxygen is slowly released along with electrons into the conducting band [23, 49]. Considering the reaction complexity of acetone [49], the total response of acetone is smaller than that of H_2S.

The degradation of the sensor response of the Pt-WO_3 fibers along with an increase in the operating temperature was identical to that shown in the acetone sensing result (Fig. 6(c)). Compared to the highest response at 350 °C, the relative H_2S responses of Pt-WO_3 fibers are greatly reduced to 1.5 % of the sensor response at 500 °C. For the IrO_2-WO_3 fibers, the highest response (R_{air}/R_{gas}=7.55, 5 ppm) to H_2S was achieved at 400 °C and the relative response rates compared to the maximum value remained almost constant (>90 %) regardless of the temperature.

Figure 6(d) shows the linear extended H_2S response of the Pt-WO_3 fibers at 350 °C. Despite the steep slope, the calculated H_2S response (R_{air}/R_{gas}=1.27) of the Pt-WO_3 fibers at 0.3 ppm can be utilized to detect exhaled H_2S, which commonly requires a detection level as low as 0.6 ppm.

The temperature-insensitivity of IrO_2-WO_3 to H_2S responses shows regular responses of H_2S for concentration

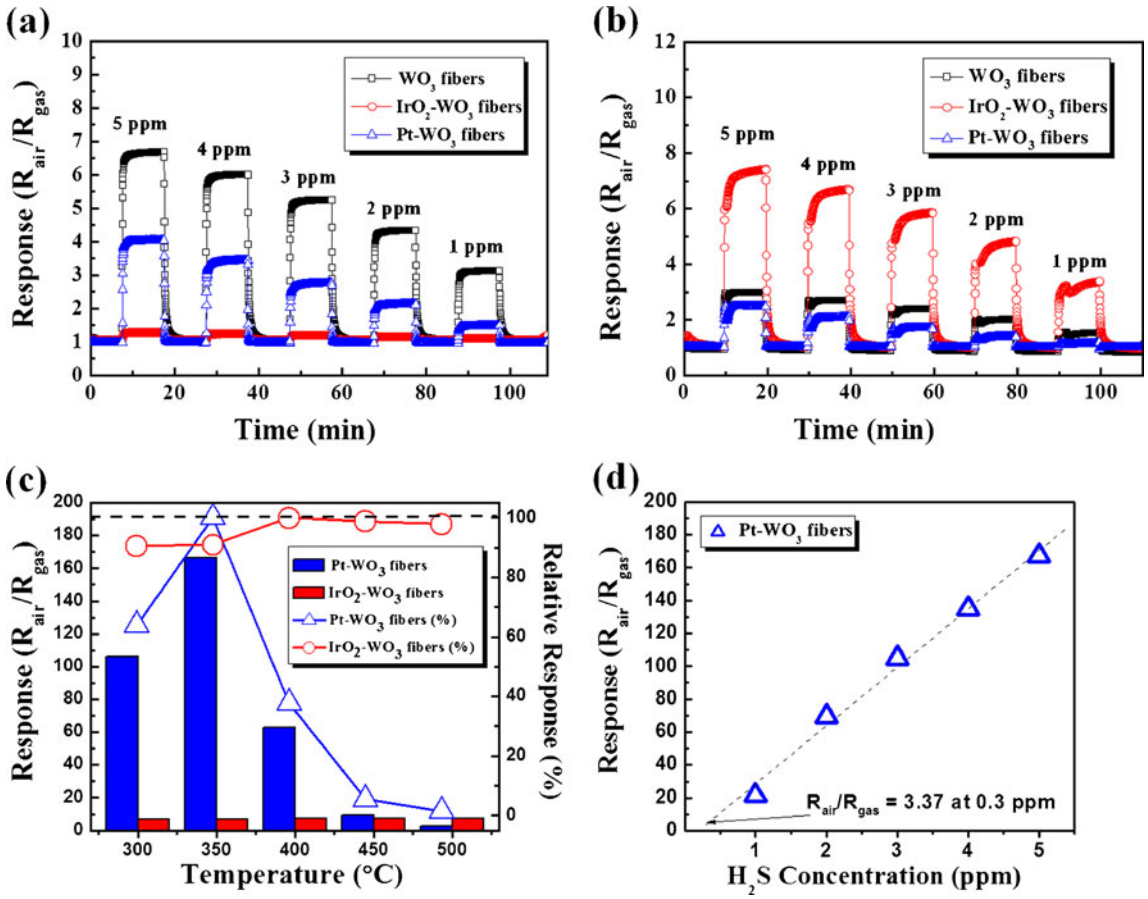

Fig. 6 The cyclic H_2S response (R_{air}/R_{gas}) of WO_3, Pt-WO_3, and IrO_2-WO_3 fibers at (**a**) 350 °C and (**b**) 500 °C under H_2S concentrations (5, 4, 3, 2 and 1 ppm). (**c**) H_2S responses of Pt-WO_3 and IrO_2-WO_3 fibers at various temperatures (350–500 °C) at 5 ppm, The inset is magnified H_2S response at 400 °C and 500 °C. (**d**) The linear extended acetone response of Pt-WO_3 fibers at 350 °C

ranges from 1 ppm to 5 ppm at 350 °C–500 °C (Fig. 7). We presume that the temperature-independent sensing properties of the IrO_2-WO_3 fibers originated from the effect of the IrO_2 catalyst, which provides near-constant resistivity irrespective of the temperature. More importantly, we expect that this phenomenon mainly results from the electrical sensitization of the catalyst and the metal oxide [45]. The resistivity changes during the electrical interactions are generated by exchanges of electrons between the metal oxide and the catalyst, where the oxygen adsorption reaction occurs on the catalyst surface rather than on the WO_3 surface [44]. With regard to this viewpoint, a large mobile carrier density of IrO_2 may serve to capture oxygen on the surface of IrO_2, thereby maintaining a certain response to H_2S irrespective of the temperature, whereas oxygen adsorption on the WO_3 surface for Pt-WO_3 and pristine WO_3 fibers is relatively more dependent on the temperature. In addition, IrO_2 has high thermal stability [42] such that the IrO_2-WO_3 fibers can maintain stable electron distributions on the surface to adsorb oxygen molecules at elevated temperatures.

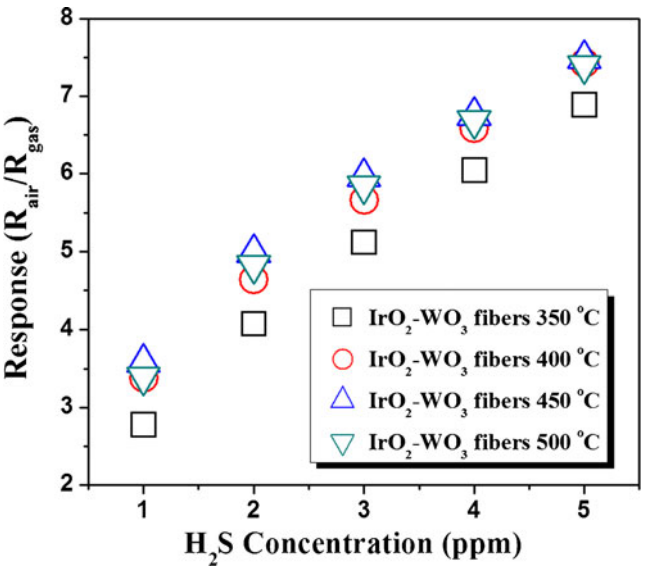

Fig. 7 The H_2S response (R_{air}/R_{gas}) of IrO_2-WO_3 fibers at various temperatures (350–500 °C) under H_2S concentrations (5, 4, 3, 2 and 1 ppm)

4 Conclusion

Polycrystalline WO_3 fibers were synthesized by electrospinning followed by calcination at 500 °C and were used to prepare chemiresistive sensors for exhaled breath analyses of diabetes and halitosis by detecting acetone and H_2S in a humid atmosphere (RH 75 %). To provide enhanced gas-sensing properties, Pt (4–7 nm) and Ir (4–8 nm) nanoparticles prepared by polyol synthesis were added to the surface of the WO_3 fibers. Whereas well-dispersed Pt particles on WO_3 fibers were revealed by TEM images, slightly agglomerated IrO_2 particles on WO_3 fibers were obtained after the post-heat-treatment step. The oxidation behaviors of both Pt and IrO_2 particles during the post-heat-treatment process were confirmed by HRTEM and XPS analyses. The p-type semiconductor property of PtO (0.86 eV) and the n-type semiconductor property of IrO_2 (2.34 eV) resulted in totally distinct sensor properties which can give rise to certain selectivity to acetone and H_2S driven by chemical sensitization and electrical sensitization, respectively. Moreover, the Pt-WO_3 fibers showed a 2.9-fold (R_{air}/R_{gas}=7.96 versus 2.74) higher acetone response at 300 °C and, more importantly, a superior H_2S response, by 19.5-fold (R_{air}/R_{gas}=106.43 versus 5.45), compared to pristine WO_3 fibers. The superior H_2S sensing capability of Pt-WO_3 fibers is clearly beneficial to those seeking to diagnosis halitosis. Although the acetone response of the WO_3 fibers ceased when they were decorated with IrO_2 particles, the benefit of the IrO_2 catalyst was its exclusive selectivity to H_2S gas. To be specific, IrO_2-WO_3 fibers which exhibit high selectivity between acetone and H_2S can be utilized as a standard reference for H_2S and acetone gases. This means that IrO_2-WO_3 fibers can effectively detect H_2S gas without any disturbance caused by acetone in exhaled breath. Considering the unique gas response characteristics of Pt-WO_3 and IrO_2-WO_3 fibers as exhaled breath sensors, it is possible to build a sensor set for accurate diagnosis of halitosis and diabetes. The interesting part of this research is that it represents the first finding of temperature-insensitive responses of IrO_2 as a catalyst. This can lead to the creation of sensors with valuable properties, especially sensors that are utilized in a wide temperature range. We anticipate that further works will be related to the optimization and control of the catalyst quantities and the unprecedented unique properties of IrO_2 catalysts.

Acknowledgments This work was supported by a grant from the Ministry of Research, Korea and the Ministry of Science & Technology, Israel. This work was also supported by the Engineering Research Center Program from Korean National Research Foundation.

References

1. S.V. Ryabtsev, A.V. Shaposhnick, A.N. Lukin, E.P. Domashevskaya, Sens. Actuators B **59**, 26 (1999)
2. J.B. Yu, H. Gi Byun, M.S. So, J.S. Huh, Sens. Actuators B **108**, 305 (2005)
3. J. Rodrıguez-Fernández, J.M.L. Costa, R. Pereiro, A. Sanz-Medel, Anal. Chem. Acta **398**, 23 (1999)
4. M. Hanada, H. Koda, K. Onaga, K. Tanaka, T. Okabayashi, T. Itoh, H. Miyazaki, Anal. Chem. Acta **475**, 27 (2003)
5. J. Rodrıguez-Fernández, R. Pereiro, A. Sanz-Medel, Anal. Chem. Acta **471**, 13 (2002)
6. D. Smith, P. Spanel, A.A. Fryer, F. Hanna, G.A.A. Ferns, J. Breath Res. **5**, 022001 (2011)
7. F. Bouillaud, F. Blachier, Antioxid. Rredox. Sign. **15**(2), 379 (2011)
8. N. Alagirisamy, S.S. Hardas, S. Jayaraman, Anal. Chem. Acta **661**, 97 (2010)
9. X. Hu, Y. Masuda, T. Ohji, K. Kato, J. Am. Ceram. Soc. **92**(4), 922 (2009)
10. L. Francioso, A.M. Taurino, A. Forleo, P. Siciliano, Sens. Actuators B **130**, 70 (2008)
11. H.S. Kim, C.H. Jin, S.H. Park, C.M. Lee, J. Electroceram. Onlie First, (2012)
12. J.Y. Park, D.E. Song, S.S. Kim, Nanotechnol. **19**, 105503 (2008)
13. Y. Dai, W. Liu, E. Formo, Y. Sun, Y. Xia, Polym. Adv. Technol. **22**, 326 (2011)
14. W. Sigmund, J. Yuh, H. Park, V. Maneeratana, G. Pyrgiotakis, A. Daga, J. Taylor, J.C. Nino, J. Am. Ceram. Soc. **89**(2), 395 (2006)
15. I.D. Kim, E.K. Jeon, S.H. Choi, D.K. Choi, H.L. Tuller, J. Electroceram. **25**, 159 (2010)
16. J.A. Park, J. Moon, S.J. Lee, S.H. Kim, T. Zyung, H.Y. Chu, Mater. Lett. **64**, 255 (2010)
17. W.Y. Wu, J.M. Ting, P.J. Huang, Nanoscale Res. Lett. **4**, 513 (2009)
18. P.I. Gouma, K. Kalyanasundaram, A. Bishop, J. Mater. Res. **21** (11), 2904 (2006)
19. L. Xu, B. Dong, Y. Wang, X. Bai, Q. Liu, H. Song, Sens. Actuators B **147**, 531 (2010)
20. S.H. Choi, I.S. Hwang, J.H. Lee, S.G. Oha, I.D. Kim, Chem. Commun. **47**, 9315 (2011)
21. G. Wang, Y. Ji, X. Huang, X. Yang, P.I. Gouma, M. Dudley, J. Phys. Chem. B **110**, 23777 (2006)
22. K. Kanda, T. Maekawa, Sens. Actuators B **108**, 97 (2005)
23. R.S. Khadayate, J.V. Sali, P.P. Patil, Talanta **72**, 1077 (2007)
24. O. Berger, W.J. Fischer, J. Mater. Sci. Mater. Electron. **15**, 463 (2004)
25. P.I. Gouma, K. Kalyanasundaram, Appl. Phys. Lett. **93**, 244102 (2008)
26. P.M. Woodward, A.W. Sleight, J Solid State Chem. **131**, 9 (1997)
27. X. Lu, X. Liu, W. Zhang, C. Wanga, Y. Wei, J. Colloid Interface Sci. **298**(2), 996 (2006)
28. S. Piperno, M. Passacantando, S. Santucci, L. Lozzi, J. Appl. Phys. **101**, 124504 (2007)
29. K.M. Sawicka, A.K. Prasad, P.I. Gouma, Sens. Lett. **3**, 31 (2005)
30. J. Leng, X. Xu, N. Lv, H. Fan, T. Zhang, J. Colloid Interface Sci. **356**, 54 (2011)
31. T.A. Nguyena, S. Park, J.B. Kim, T.K. Kim, G.H. Seong, J. Choo, Y.S. Kim, Sens. Actuators B **160**, 549 (2011)
32. M. Righettoni, A. Tricoli, S.E. Pratsinis, Anal. Chem. **82**, 3581 (2010)
33. L. Wang, A. Teleki, S.E. Pratsinis, P.I. Gouma, Chem. Mater. **20**, 4794 (2008)
34. L. Wang, X. Yun, M. Stanacevic, P.I. Gouma, AIP Conf. Proc. **1137**, 206 (2009)
35. J. Tamaki, Y. Michiba, S. Kajita, IEEJ Trans. Sens. and Micromach. **128**(4), 145 (2008)

36. Y.S. Kim, K. Lee, J. Nanosci. Nanotechnol. **9**, 2453 (2009)
37. F. Bonet, V. Delmas, S. Grugeon, R. Herrera Urbina, P.Y. Silvert, Nanostruct. Mater. **11**(8), 1277 (1999)
38. H. Kang, Y. Zhu, Y. Jing, X. Yang, C. Li, Colloids Surf. A: Physicochem. Eng. Aspects **356**, 120 (2008)
39. S. Koombhongse, W. Liu, D.H. Reneker, J. Polym. Sci., Part B: Polym. Phys. **39**, 2598 (2001)
40. R.S. Chen, H.M. Chang, Y.S. Huang, D.S. Tsai, S. Chattopadhyay, K.H. Chen, J. Cryst. Growth **271**, 105 (2004)
41. K.W. Park, Y.E. Sung, J. Appl. Phys. **94**(11), 7276 (2003)
42. N.V. Hullavarad, S.S. Hullavarad, IEEE Trans. Nanotechnol. **9**(5), 625 (2010)
43. D.S. Vlachos, C.A. Papadopoulos, J.N. Avaritsiotis, Appl. Phys. Lett. **69**, 650 (1996)
44. D.S. Vlachos, C.A. Papadopoulos, J.N. Avaritsiotis, Sens. Actuators B **44**, 458 (1997)
45. S. Matsusima, Y. Teraoka, N. Miura, N. Yamazoe, Jpn. J. Appl. Phys. **27**(10), 1798 (1988)
46. S. Liu, F. Zhang, H. Li, T. Chen, Y. Wang, Sens. Actuators B **162**, 259 (2012)
47. H.M. Lin, C.M. Hsu, H.Y. Yang, P.Y. Lee, C.C. Yang, Sens. Actuators B **22**, 63 (1994)
48. T. Maosong, D. Guorui, G. Dingsan, Appl. Surf. Sci. **171**, 226 (2001)
49. P.P. Sahay, J. Mater. Sci. **40**, 4383 (2005)